



HAL
open science

Structural evidence for a new elaborate 3D-organization of the cardiomyocyte lateral membrane in adult mammalian cardiac tissues

Celine Guilbeau-Frugier, Marie Cauquil, Clement Karsenty, Camille Dambrin, Bruno Payre, Hervé Cassard, Claudie Josse, Marie-Hélène Seguelas, Sophie Allart, Maxime Branchereau, et al.

► To cite this version:

Celine Guilbeau-Frugier, Marie Cauquil, Clement Karsenty, Camille Dambrin, Bruno Payre, et al.. Structural evidence for a new elaborate 3D-organization of the cardiomyocyte lateral membrane in adult mammalian cardiac tissues. *Cardiovascular Research*, 2019, 115 (6), pp.1078-1091. 10.1093/cvr/cvy256 . hal-02321816

HAL Id: hal-02321816

<https://hal.science/hal-02321816>

Submitted on 21 Oct 2019

HAL is a multi-disciplinary open access archive for the deposit and dissemination of scientific research documents, whether they are published or not. The documents may come from teaching and research institutions in France or abroad, or from public or private research centers.

L'archive ouverte pluridisciplinaire **HAL**, est destinée au dépôt et à la diffusion de documents scientifiques de niveau recherche, publiés ou non, émanant des établissements d'enseignement et de recherche français ou étrangers, des laboratoires publics ou privés.

Structural evidence for a new elaborate 3D-organization of the cardiomyocyte lateral membrane in adult mammalian cardiac tissues

Céline Guilbeau-Frugier^{1,2,3†}, Marie Cauquil^{1†}, Clément Karsenty^{1,4,5}, Olivier Lairez^{1,4}, Camille Dambrin⁴, Bruno Payré³, Hervé Cassard⁶, Claudie Josse⁷, Marie-Hélène Seguelas¹, Sophie Allart⁸, Maxime Branchereau¹, Christophe Heymes¹, Franck Mandel¹, Marie-Bernadette Delisle^{3,9}, Atul Pathak^{1,10}, Etienne Dague¹¹, Jean-Michel Sénard^{1,12}, and Céline Galés^{1*}

¹Institut des Maladies Métaboliques et Cardiovasculaires, Université de Toulouse, INSERM U1048, I2MC, 1, Avenue Jean Poulhès—BP84225, 31432 Toulouse, France; ²Department of Forensic Medicine, Centre Hospitalier Universitaire de Toulouse, Université de Toulouse, Toulouse, France; ³Centre de Microscopie Électronique Appliquée à la Biologie, Faculté de Médecine Rangueil, Université de Toulouse, Toulouse, France; ⁴Department of Cardiology, Centre Hospitalier Universitaire de Toulouse, Toulouse, France; ⁵CHU Toulouse, Pediatric and Congenital Cardiology, Children's Hospital, Université de Toulouse, Toulouse, France; ⁶UMR IHAP, Université de Toulouse, INRA, ENVT, Toulouse, France; ⁷Centre de MicroCaractérisation Raimond Castaing, UMS 3623, Toulouse, France; ⁸Centre de Physiopathologie de Toulouse-Purpan, Université de Toulouse, INSERM, CNRS, Toulouse, France; ⁹Department of Histopathology, Centre Hospitalier Universitaire de Toulouse, Université de Toulouse, Toulouse, France; ¹⁰Department of Cardiovascular Medicine, Hypertension, Risk Factors and Heart Failure Unit, Clinique Pasteur, Toulouse, France; ¹¹LAAS-CNRS, Université de Toulouse, CNRS, Toulouse, France; and ¹²Department of Clinical Pharmacology, Centre Hospitalier Universitaire de Toulouse, Université de Toulouse, Toulouse, France

Received 12 February 2018; revised 29 June 2018; editorial decision 23 September 2018; accepted 11 October 2018; online publish-ahead-of-print 17 October 2018

Time for primary review: 45 days

Aims

This study explored the lateral crest structures of adult cardiomyocytes (CMs) within healthy and diseased cardiac tissue.

Methods and results

Using high-resolution electron and atomic force microscopy, we performed an exhaustive quantitative analysis of the three-dimensional (3D) structure of the CM lateral surface in different cardiac compartments from various mammalian species (mouse, rat, cow, and human) and determined the technical pitfalls that limit its observation. Although crests were observed in nearly all CMs from all heart compartments in all species, we showed that their heights, dictated by the subsarcolemmal mitochondria number, substantially differ between compartments from one species to another and tightly correlate with the sarcomere length. Differences in crest heights also exist between species; for example, the similar cardiac compartments in cows and humans exhibit higher crests than rodents. Unexpectedly, we found that lateral surface crests establish tight junctional contacts with crests from neighbouring CMs. Consistently, super-resolution SIM or STED-based immunofluorescence imaging of the cardiac tissue revealed intermittent claudin-5-claudin-5 interactions *in trans* via their extracellular part and crossing the basement membrane. Finally, we found a loss of crest structures and crest–crest contacts in diseased human CMs and in an experimental mouse model of left ventricle barometric overload.

Conclusion

Overall, these results provide the first evidence for the existence of differential CM surface crests in the cardiac tissue as well as the existence of CM–CM direct physical contacts at their lateral face through crest–crest interactions. We propose a model in which this specific 3D organization of the CM lateral membrane ensures the myofibril/myofiber alignment and the overall cardiac tissue cohesion. A potential role in the control of sarcomere relaxation and of diastolic ventricular dysfunction is also discussed. Whether the loss of CM surface crests constitutes an initial and common event leading to the CM degeneration and the setting of heart failure will need further investigation.

Keywords

Cardiomyocyte • Lateral membrane • Cardiac tissue architecture • Subsarcolemmal mitochondria • Electron-atomic force microscopy • Sarcomere relaxation

* Corresponding author. Tel: +33 5 31 22 40 75; fax: +33 5 61 32 56 16, E-mail: celine.gales@inserm.fr

† The first two authors contributed equally to this work.

1. Introduction

The adult cardiac tissue cohesion necessary for the continuous cyclic mechanical strain mainly relies on a substantial three-dimensional (3D) interaction between contractile cardiomyocytes (CMs) and the extracellular matrix (ECM). Interestingly, CMs undergo different morphological adaptations during heart development. Throughout embryonic and early postnatal developmental stages, CMs exhibit a plastic phenotype with a round or spindle-fibroblastic shape that correlates with their proliferative state and contributing to the increase of heart mass through hyperplasia. At approximately Day 5 postnatal in rodents, CMs stop proliferating and initiate a maturation step to acquire their typical adult rod-shape.¹ Within the tissue, this rod-shaped cell morphology is stabilized through specific and direct CM–CM interactions via the intercalated disk (ID) localized at the bipolar ends of the CM, while the lateral cell surface is classically believed to interact with the ECM through receptors (integrin/dystroglycan) on the costamere, without physical contacts between proximate CMs.² Both surface structures control the CM contraction with the ID underlying the physical anchorage of the contractile myofibrils and contraction synchronization via gap junctions and the lateral membrane, relaying ECM extracellular signals to the myofibrils for contractile adaptation to the cardiac pressure load.

More recently, we and other groups have identified that cell–cell communication transmembrane proteins, i.e. Ephrin-B1³ and Claudin-5⁴ have an atypical expression on the lateral sarcolemmal membrane of adult CMs and act independently on the contractile apparatus, thus suggesting that the functions of the lateral membrane are not completely understood. These findings subsequently prompted us to explore the lateral membrane at a high resolution in mice, and using atomic force microscopy (AFM), we identified a highly organized cell surface architecture of the CMs with the presence of periodic stiff crests related to the presence of subsarcolemmal mitochondria (SSM), which were lost following ischaemia.⁵ Similar highly organized crest structures and their disorganization in heart failure have been reported indirectly by analysing the CM ionic surface profile via scanning ion conductance microscopy.^{6,7} However, to date, these studies have mainly relied on the analysis of isolated adult CMs. Whether the presence of well-defined crest structures at the CM surface is a general feature of all heart compartments and how they organize within the cardiac tissue remain unknown.

Herein, we explored the lateral membrane of CMs in cardiac tissue samples from different heart compartments that originated from various mammalian species using high-resolution scanning or cryo-scanning and transmission electron microscopy (TEM), as well as AFM. We first identified a compartment- and species-dependent crest architecture at the CM surface. More strikingly, we noted the presence of intermittent tight junctions between crests from adjacent CMs in mammals including humans, thus establishing for the first time proof of the concept of existence of a physical interaction between lateral membranes of adjacent CMs. This discovery brings to the fore the complexity of the 3D-structure of the adult CMs in the tissue and should open a new research area to decipher the functional relevance of these lateral contacts in cardiac physiology and pathophysiology.

2. Methods

2.1 Animal models and cardiac tissue processing

Studies were performed on 2-month-old male C57BL/6J OlaHsd mice and WistarRccHan rats (purchased from Envigo, Huntingdon, UK). The experimental animal protocols were carried out in accordance with

the European and French regulation guidelines for animal experimentation and were approved by the local ethical committee. Mice and rats were euthanized through an intraperitoneal injection of pentobarbital sodium (160 mg/kg), while 50 mg/kg was used for the KCl experiments.

To stop the heart in diastole, KCl (1 M) was directly injected as a bolus in the inferior vena cava in anaesthetized and thoracotomized mice. After arrest, the hearts were immediately removed, and sections (~1 mm³) were fixed in 2% glutaraldehyde in cold Sorensen's buffer for further electron microscopy analysis.

For cardiac tissue processing on ice, immediately after removal, the heart was plunged in cold PBS for several seconds, thus instantly stopping the heartbeat. The heart was then cautiously sliced (~1 mm³) on an ice bed without torsion or pressure and fixed in 2% glutaraldehyde in Sorensen's buffer at 4°C for further electron microscopy analysis.

For transcardial fixative perfusion, immediately after removal from the chest, the heart was plunged in cold PBS for several seconds thus instantly stopping the heartbeat. The aorta was then first retroperfused with cold phosphate buffer saline with a peristaltic pump (0.3 mL/min) for 3 min followed by 3 min of retroperfusion with cold 2% paraformaldehyde/0.1% glutaraldehyde. The heart sections (~1 mm³) were subsequently fixed in 2% glutaraldehyde in cold Sorensen's buffer for further electron microscopy analysis.

For the cow study, two 8-year-old Blonde d'Aquitaines (weight 770 kg) were analysed in collaboration with the Veterinary National School of Toulouse (ENVT). They were euthanized with a barbiturate injection due to a bilateral pyelonephritis and a chronic abscess on the paws. Immediately after bleeding, the heart was removed and sections (~1 mm³) were fixed in 2% glutaraldehyde in Sorensen's buffer at 4°C for further electron microscopy analysis.

2.2 Transaortic constriction (TAC) and echocardiographic assessment

Two-month-old male C57BL/6J Crl mice were used for these experiments. The mice were housed with a 12:12 light-dark cycle and fed *ad libitum* with standard chow and water. Thoracic aortic constriction (TAC) was performed on mice anaesthetized with 1% isoflurane. After endotracheal intubation, the mice were connected to a rodent ventilator. The transverse aorta was isolated and TAC was performed by tying a nylon suture ligature against a 26-gauge needle, the latter being promptly removed to induce pressure overload cardiac hypertrophy. After aortic constriction, the chest was closed and the pneumothorax was evacuated. After extubation, the mice were allowed to recover from the anaesthesia. Sham operated animals (controls) underwent the same operation except for the performance of aortic constriction. Fifteen days after surgery, animals underwent non-invasive transthoracic echocardiography using a Vevo[®] 2100 device (VisualSonics) under 1% isoflurane anaesthesia. Cardiac wall thickness and ejection fraction were measured at least three times for each animal in M-mode images and in long-axis B-mode, respectively. All measurements were obtained by an investigator blinded to the genotype of the animals.

2.3 Human tissue samples

Human cardiac appendages from the tissue collection of the Toulouse University Hospital (registered according to French regulations for clinical research-DC 2009-989) were analysed after patients consented to their use. All patients were Caucasian and had undergone extracorporeal circulation for cardiac surgery performed at Toulouse University hospital (Table 1). Within 1 h of the removal, the appendages were isolated and 1 mm³ pieces were directly fixed in 2% glutaraldehyde in

Table 1 Clinical data for human heart samples

Patient	Gender	Age (years)	Cause of surgery	Collected tissue	LVEF (%)	Others
1	Female	80	Coronary bypass	RAp	Normal	–
2	Male	70	Mitral and tricuspid valves flail	LAp	Normal	Dilated RVPAH
3	Male	68	Aortic valve stenosis	RAp	Normal	Dilated atria
4	Female	60	Mitral valve stenosis	LAp	40%	Dilated LA
5	Male	69	Mitral valves flail	LAp	Normal	Dilated LA and LV
6	Male	59	Cardiac transplantation for arrhythmogenic right ventricular dysplasia	LV	Normal	Dilated RV

LA, left atrium; LAp, left appendage; LV, left ventricle; LVEF, left ventricle ejection fraction; PAH, pulmonary arterial hypertension; RA, right atrium; RAp, right appendage; RV, right ventricle.

Sorensen's buffer at 4°C prior to inclusion and further electron microscopy analysis.

2.4 Cardiomyocyte purification from adult rats

For the AFM study, CMs were isolated from adult rats using the Langendorff perfusion method as previously described.⁵ Beating hearts were quickly removed from the chest after intra-peritoneal injection of pentobarbital (160 mg/kg) and Langendorff perfused with Krebs solution (in mM: NaCl 113, KCl 4.7, KH₂PO₄ 0.6, NaHPO₄ 0.6, MgSO₄ 1.2, NaHCO₃ 12, KHCO₃ 10, HEPES 10, taurin 30, 2,3-butanedione monoxime (BDM) 10, glucose 5.5, pH 7.4) containing 0.5 mM CaCl₂ at 37°C for 6 min. Perfusion was then switched to a decalcifying solution (Krebs solution containing 0.1 mM EGTA) at 37°C for 2 min. Finally, the perfusion was switched to an enzymatic solution (Krebs solution containing 2.2 mg/mL Type II collagenase-Worthington Biochemical corporation) and 12.5 μM CaCl₂ at 37°C for 20 min. Following digestion, the left and right free wall ventricles were separated and dissected into 1 mm³ pieces. The myocytes were mechanically dissociated using Pasteur pipette in resuspension solution (Krebs solution containing 10% bovine calf serum and 12.5 μM CaCl₂). The myocyte suspension was then filtered through a 200 μm mesh and harvested after sedimentation. The isolated myocytes were plated for 10 min on specific laminin (mouse laminin, Life technology)-coated culture dishes (40 × 11 mm, TPP-Tissue Culture treated dishes) in the resuspension solution at 37°C (5% CO₂). CMs were then fixed in 2% glutaraldehyde in Sorensen's buffer for 10 min at room temperature, washed three times with PBS and immediately used for the AFM experiments in PBS.

2.5 Transmission and scanning electron microscopy (TEM-SEM)

Heart samples were fixed by immersion in 2% glutaraldehyde in Sorensen's buffer at 4°C and processed for TEM or scanning electron microscopy (SEM) as previously described.⁵

All crest height and sarcomere length measurements were performed on TEM micrographs. The crest heights were measured from the top of the crest to the first myofibril top layer using Fiji software and the SSM number was quantified for each crest. The sarcomere lengths were measured similarly on the first myofibril layer below the CM surface crests.

2.6 Cryo-scanning electron microscopy

After fixation, as indicated for the SEM procedure, the samples were incubated for 12 h in cryo-protectant glycerol and rapidly frozen in nitrogen

slush at -220°C. The frozen samples were transferred under vacuum to the cryo-chamber apparatus (Quorum PP3000T) at -140°C and fractured with a cold knife integrated in the cryo-chamber. The temperature was increased to -95°C and maintained for 10 min of sublimation and the specimen was then coated with platinum by sputtering (60 s, 10 mA) and moved in the high vacuum mode into the SEM observation chamber of a FEI Quanta 250 FEG scanning electron microscope (5 kV). The specimen was maintained at a temperature less than -140°C at all procedure steps.

2.7 Dual beam (SEM+FIB) 3D reconstitution microscopy

The 3D-characterization of the CM lateral membrane was carried out using Focused Ion Beam (FIB) tomography. This method was developed using the dual beam system Helios NanoLab 600i (FEI company). The instrument incorporates both a FIB and a field emission scanning electron microscope (FEG-SEM).

The myocardial heart sample was processed similarly as the SEM until resin embedding and then introduced into the FIB-SEM chamber. The sample was covered with a conductive layer of platinum to avoid surface charging and protect it from the ion beam (30 kV, 2.5 nA). Dual-beam scanning was conducted on 300 sequential sample slices (50 nm thick) with SEM image acquisition for each slice (5 kV voltage, 0.69 nA current, TLD detector). Three-dimensional reconstitution of the heart myocardium sample was conducted using AVIZO software (FEI).

2.8 Atomic force microscopy

Surface images of fixed isolated rat CMs were recorded in PBS buffer in Quantitative Imaging™ mode⁸ with MLCT AUWH (Bruker) cantilevers (nominal spring constant of 0.01 N/m) and using an AFM Nanowizard III (JPK Instruments, Berlin, Germany). The applied force was maintained at 3 nN and the Z length to 5 μm. Therefore, the loading rate was 2 500 000 pN/s (acquisition frequency of the force curves is 25 Hz). The cantilever spring constants were determined by the thermal noise method. For all results presented in this study, the silicon nitride AFM tips were bare. AFM topographical images were analysed using the JPK data processing software. The crest heights were measured based on a manual cross-section delimitation perpendicular to the CM myofilaments and considering the base line as the position of the plasma membrane in the absence of crests. Membrane holes, due to fixative artefacts, were not considered for height measurements.

2.9 Immunofluorescence imaging

All imaging data was obtained using frozen cardiac tissue sections fixed in acetone, except for collagen III-SIM imaging (paraffin-embedded heart sections). Heart sections were immunostained using standard protocols with

the following primary antibodies incubated overnight at 4°C: anti-laminin 2 α (Abcam, ab11576), anti-claudin-5 (Acris, DP157), anti-collagen III (Acris, BP8014), anti- α -actinin (Abcam ab68167), anti-cardiac Troponin T (Life Technologies, MA5-12960). Heart sections were rinsed three times with PBS and labelled with secondary antibodies (Oregon Green 488 goat anti-rabbit IgG, Life Technologies O11038; AlexaFluor 594 goat anti-rat IgG, Life Technologies A11007; STAR RED goat anti-rabbit, Sigma 41699) and Texas-Red (Life Technologies, W21405)- or Oregon Green 488 (Life Technologies, W6748) conjugated Wheat-Germ-Agglutinin for 1 h at room temperature. Coverslips were finally mounted on microscopy slides using Mowiol.

Confocal imaging was carried out using a Zeiss LSM 780 confocal microscope and Zen 2011 software (Carl Zeiss).

Super-resolution structured illumination microscopy (SR-SIM) was carried out on aELYRA PS.1 (Carl Zeiss), lasers 488, 561, and/or 642 nm with a Plan Achromat 63 \times /NA 1.46 oil objective and a grid size of 32 or 42 μ m equipped with a sCMOS PCO Edge camera. Image stacks of several micrometer thicknesses were taken with 0.110 μ m z-steps, five phases and three rotations per z-section. Reconstruction of images was performed using Zeiss Zen 2.1 software and a Noise Filter.

Super-resolution stimulated emission depletion (SR-STED) microscopy images were acquired using a Leica SP8 STED 3 \times microscope (Leica Microsystems, Germany) and a 100 \times NA: 1.4 oil immersion objective. To optimize the resolution without bleaching in 3D, the 775 nm STED laser line was applied at the lowest power that can provide sufficient improvement in resolution compared with confocal. Z-stack series were acquired sequentially with the pulsed 532 nm laser line and the pulsed 635 nm laser line. With such settings, lateral and axial resolutions of 130 nm could be reached for both acquisition channels. For image acquisition, we used the following parameters: 43 nm pixel size, two time average per line, 400 Hz scan speed. STED images were subsequently deconvolved with Huygens Professional (SVI, USA) using the CMLE algorithm, with a signal to noise ratio (SNR) of 7. Three-dimensional visualization and reconstruction using Imaris software (Bitplane, Switzerland).

2.10 Quantification of CM area

For *in situ* quantification of the CM surface area, deparaffinized heart slides were stained with Texas Red-conjugated-WGA (Life technologies, W21405) and both CM area and density were measured in heart cross-sections by manually tracing the cell contour on images of whole hearts acquired on a digital slide scanner NanoZoomer (Hamamatsu) using NDP.view2 viewing software. The experimenter was blinded to the mouse group.

2.11 Statistics

All bar graphs represent means \pm s.e.m. Statistical analyses were performed using Prism v5 software. Statistical significance was calculated using Student's *t*-test (Figures 2B, C, H, 3B, E, 5B), two-way ANOVA (Figure 2D), Spearman correlation test (Figure 2E, G), or Fisher's exact test (Figure 5C). **P* < 0.05, ***P* < 0.01, ****P* < 0.001.

3. Results

3.1 Intricate 3D-CM surface crest architecture in cardiac tissues of different mammalian species and technical pitfalls

In general, the cardiac tissue structure is inferred from a histological analysis commonly performed on formol-fixed hearts and paraffin

embedded sections, thus preventing appreciation of the CM 3D-structure and organization. Here, we first processed samples from the left ventricles (LV) of adult male mouse hearts (2 months old) using SEM to visualize at a high resolution, the 3D-morphology of the CM surface within the tissue. In the left ventricular myocardium, we found that the circumference of the CM lateral surface is covered by highly organized periodic rows of bulged structures in contact with the ECM (Figure 1A, upper panels). These elongated structures are orientated perpendicularly with regard to the longitudinal intracellular myofibrils. In a second set of experiments, samples were processed for cryo-SEM to enable visualization of the CM intracellular components through cell transversal sectioning. In this context, the CM surface noticeably appears as a periodic alternation of crests filled with SSM tightly attached to the endoplasmic reticulum, as previously described using TEM⁵ (Figure 1A, lower panels). Similar structures were identified in the cow-LV myocardium (Figure 1B, upper left panel and Supplementary material online, Figure S1) as well as in the rat-LV and human-LV (Supplementary material online, Figure S1). Consistent with these observations of surface bulged rows, sequential 3D-reconstructions of the SEM images by dual-beam microscopy in the mouse indicated that SSM adopt an elongated morphology beneath the sarcolemma (Figure 1C). Noticeably, the periodicity of the crest rows relies on their lateral anchorage to the Z-lines that delimit each sarcomere from the outer myofibril layer (Figure 1B, upper middle panel and Supplementary material online, Figure S1, Cow-LV), more visible in TEM (Figure 1D), which we previously described as CM surface 'hollows'.⁵

It is important to note that the visualization of CM surface crest structures and intracellular SSM analysis using TEM are extremely dependent on the handling procedure of the cardiac tissue. First, the animal euthanasia method is fundamental. Specifically, cervical dislocation, as recently described for SSM observation,⁹ leads to a complete SSM loss (not shown), most likely as a consequence of cardiac fibrillation, thus precluding its use. Euthanasia using potassium chloride intra-cardiac injection, classically recommended to observe the sarcomere ultrastructure, also destroys the crest architecture (Supplementary material online, Figure S2A), most likely due to its substantial impact on sarcomere relaxation, in some cases associated with cardiac spasms. Another critical step is the delay between tissue handling after cardiac arrest and fixation for electron microscopy that must be as short as possible since, in contrast with interfibrillar mitochondria (IFM), SSM are highly prone to shrinking during tissue removal. Intra-aortic paraformaldehyde/glutaraldehyde fixative perfusion, considered to efficiently preserve soft tissues, tends to increase the lateral interspace between two CMs because of vasculature dilatation, even at the lowest perfusion flow rate, and conversely decreases crest height ('flattened-like' crests) due to substantial reductions in the SSM volume (Supplementary material online, Figure S2B). However, this latter technique is ideal for visualizing the SSM ultrastructure. Finally, in accordance with the well-known sensitivity of the heart to both protease activity and temperature, the optimal procedure for crest-SSM observation in TEM relies on the use of an ice-cold buffer immediately after tissue removal and on tissue dissection on ice, even if sarcomeric details, such as the I-band of the Z-lines cannot be systematically visualized due to arbitrary heart arrest in a contractile or relaxed state (Supplementary material online, Figure S2C). These technical pitfalls indicate that crest-SSM observation within the tissue requires specific handling of cardiac biopsies, which most likely account for the chaotic organization of the CM surface and SSM often described in the literature, as well as the discrepancies in observations between studies.

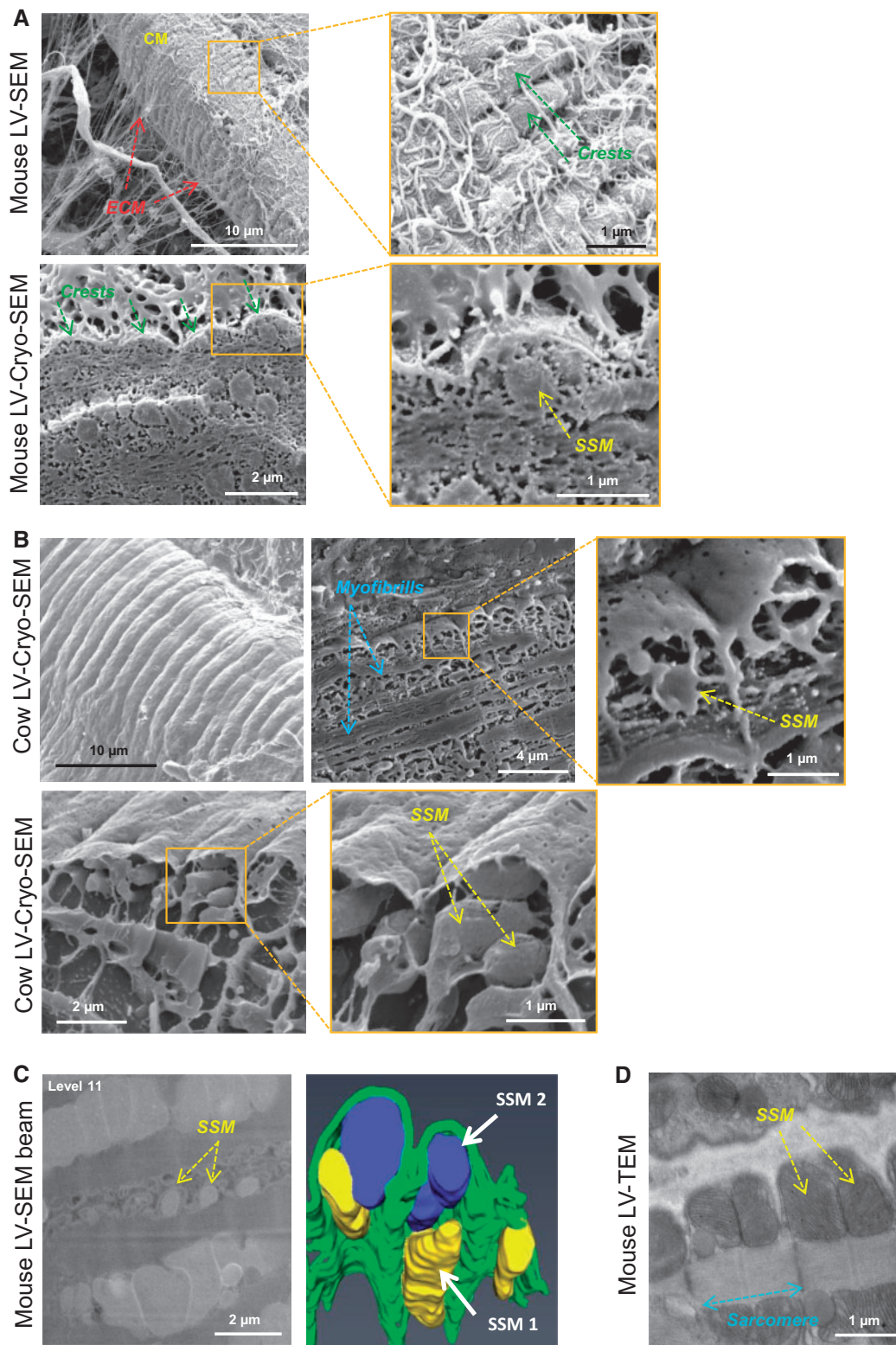


Figure 1 Lateral surface of adult cardiomyocytes (CM) exhibits crest architecture in left ventricular myocardial tissue. (A and B) Scanning electron microscopy (SEM) (A) or SEM after cryo-fracture (cryo-SEM) (B) micrographs of mouse- (A) or cow- (B) left ventricular cardiac tissue show covering of CM surface by rows of elongated structures filled with SSM. (C) Dual beam-SEM and 3D-reconstruction images of CM lateral surface (over 15 μm thick) from mouse-LV cardiac tissue show elongated SSM morphologies. (D) TEM of mouse-LV shows SSM in cell surface crests anchored to lateral Z-lines of sarcomeres.

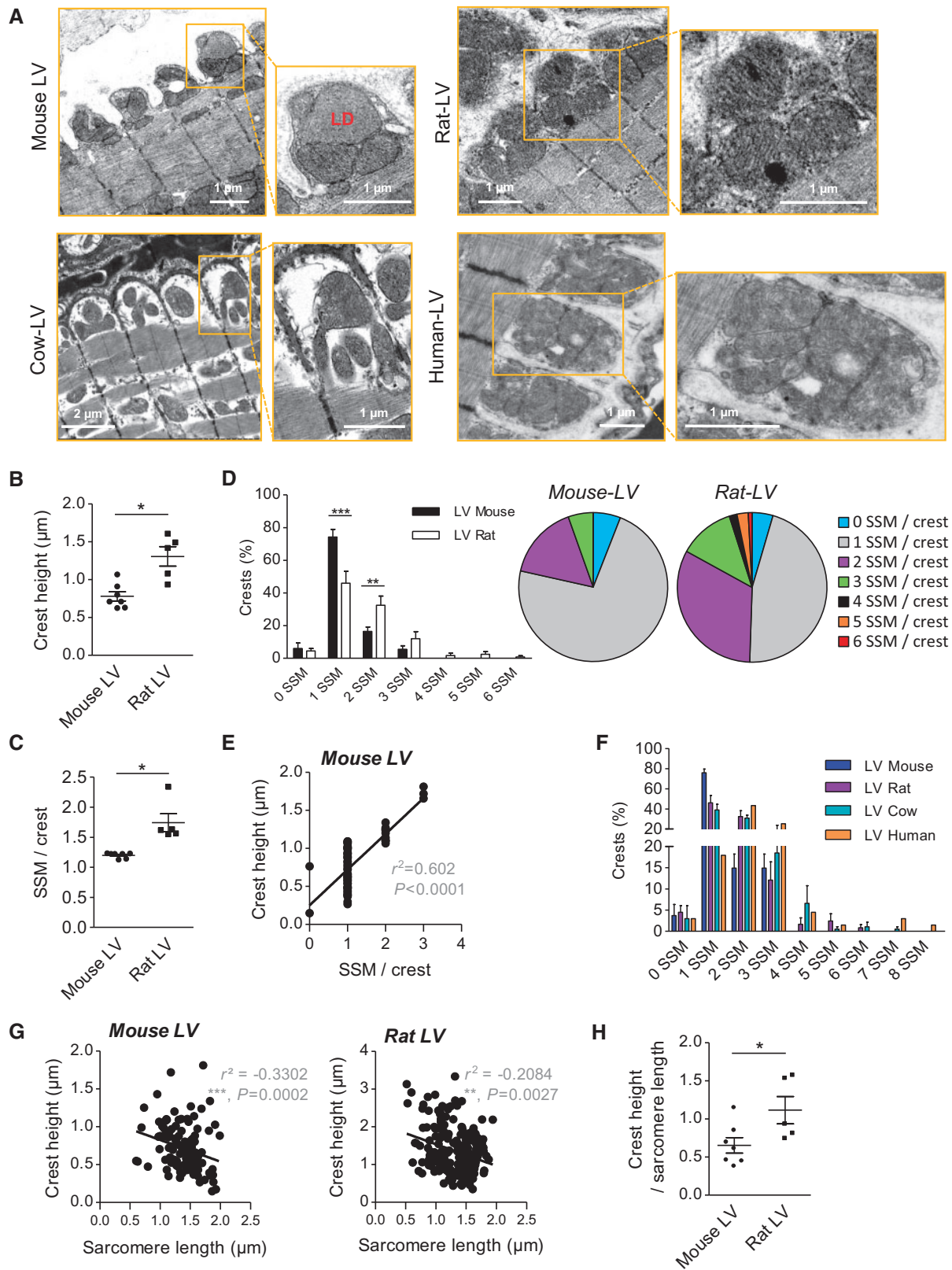


Figure 2 CM lateral surface crest relief in LV differs among adult mammalian species. (A) TEM micrographs showing representative CM surface crest relief and associated SSM from mouse-, rat-, cow-, or human-LV (*Patient 6*). LD, lipid droplet. (B–C) Quantification of crest heights (B) and SSM number/crest (C) from TEM micrographs ($n = 7$ mice, 3–7 CMs/mouse, 135 crests or $n = 5$ rats, 3–10 CMs/rat, 230 crests). The statistical significance between mouse and rat LV was assessed using unpaired Student's *t*-test (* $P < 0.05$). (D) Quantification of crest subpopulations according to their SSM number content ($n = 7$ mice and 5 rats) (left panel). The statistical significance between mouse and rat LV was assessed using two-way ANOVA followed by a Bonferroni post-test (* $P < 0.05$; *** $P < 0.001$). (Right panel) Pie chart representation of CM surface crest subpopulations. (E) Linear correlation between crest height and SSM

3.2 CM surface crest architecture in cardiac tissue is species-dependent

We subsequently investigated whether the CM surface crest architecture in the LV was similar in different mammalian adult species. TEM was thus conducted on different biopsies from LVs obtained from adult mice, rats, cows, and humans (Figure 2A). In the two latter cases, the management was less flexible than in rodents since the biopsies could not be handled in optimized conditions for crests-SSM observation. However, despite these technical pitfalls, clear differences between species were identified and quantified. When initially considering cardiac LV samples from mice, we quantified the crest height and SSM number/crest. The TEM measurements indicated average crest heights of approximately 1 μm ($0.87 \mu\text{m} \pm 0.07$; Figure 2B) with a majority of the crest populations with 1–2 SSM per crest (Figure 2C and D) and the crest height correlated with the SSM number (Figure 2E). In contrast, the crests from rat left ventricular biopsies can reach heights up to 1.5 μm ($1.31 \mu\text{m} \pm 0.13$; Figure 2B) and exhibited a higher average number of SSM per crest (Figure 2C) with a majority of the crest population with 2–3 SSM (Figure 2D and Supplementary material online, Figure S3). Even if in the minority, we also identified some crests with 4–6 SSM in the rats that were never observed in the mice. Interestingly, despite statistical quantification due to low sample numbers, cow and human left ventricular biopsies demonstrated higher crest heights within the tissue than in mice or rats and proportionally less crest populations with 1 SSM to the advantage of populations with 2, 3 and a higher SSM number (Figure 2F). Thus, in the LV, the CM surface crest heights and associated SSM number depend on the mammal species.

The insertion of CM surface crests on either Z-line side of the sarcomere highly suggested that the crests could have a role on the sarcomere contractile state. Supporting this hypothesis, and based on the MET images quantification in mice and rats, we found a significant correlation between the crest height and the sarcomere length (Figure 2G). Given that the cardiac biopsies are indifferently removed in the diastolic or systolic phase of the cardiac cycle for the MET observations, the crest heights should thus be better quantified, relative to the sarcomere length, to compensate for this contingency. As shown in Figure 2H, the correction of the crest height measurements confirmed the difference that we previously described between the mouse and rat LV (Figure 2B).

3.3 CM surface crest architecture is cardiac compartment-dependent

In cell biology, the cell structure is generally dedicated to its function. Given that each heart compartment harbours different and specific functions, we questioned the potential difference in the CM surface crest architecture in between compartments. Cryo-SEM and TEM were conducted on biopsies from the right ventricle (RV) and right atrium (RA) or the appendage (Ap) from mouse, rat, cow, and human hearts, while accurate quantifications were performed in rats. Noticeably, the 3D-CM surface relief architecture was less pronounced in the RV than in the LV as illustrated in the mice and cows in TEM-SEM micrographs

(Figures 3A, 2A, 1A and B and Supplementary material online, Figure S4). In agreement, within the tissue, the CM crest heights were significantly lower in the rat's RV than in the LV (Figure 3B) and correlated with the presence of low number of SSM/crest (Figure 3C). In particular, we measured a significant increase in the crest populations with 1 SSM/crest (RV: $\sim 68\%$; LV: $\sim 46\%$) and we also identified an important percentage of SSM-free-crests (0 SSM; RV: 15%; LV: 4.5%). In contrast, the crest populations with 2 SSM were significantly reduced (RV: $\sim 14\%$; LV: $\sim 32.5\%$), while the crest populations above 4 SSM could not be detected compared with the LV. Similar lower crest heights were identified in the RV from cows (Supplementary material online, Figure S4A).

To confirm this *in situ* observation, we quantified surface crest heights using AFM on CMs isolated from the rat RV or LV. Due to the natural de-differentiation of purified adult living CMs in culture and the relatively rapid loss of crest structures in living CMs during the AFM acquisition time we previously described,⁵ we analysed CMs fixed immediately after purification. Different fixators have been tested, however, only a short fixation in 2% glutaraldehyde was consistent with the overall surface crest preservation. In particular, we identified surface bulged rows as visualized in cryo-SEM tissue sections in the CMs from both the LV and RV (Figure 3D). The AFM-based quantifications of the crest height in the CMs isolated from the RV or LV were also highly consistent with the MET quantifications in tissue with significantly higher crests in the LV than in the RV (Figure 3E). However, the raw values highly differed between MET- (tissue) and AFM- (isolated CMs) quantifications. This discrepancy most likely relies on the stabilization of CM crests within the 3D-tissue, while isolated CMs rapidly derived and lost this structure ('SSM shrinking') in culture. This observation reinforces the notion that isolated adult CMs harbour different features than those within the tissue.

With respect to the different cardiac compartments, the CMs from mouse RA exhibited a flat and smooth sarcolemmal surface (Supplementary material online, Figure S4B, upper panels). Accordingly, at the subcellular level, although the surface crests could be perceived in TEM by their lateral anchorage to the Z-lines, they were free of 3D relief due to the lack of SSM. In contrast, the cow-RA constantly exhibited a 3D relief at the CM surface with 1–2 SSM/crest, thus resembling the RV (Supplementary material online, Figure S4B, lower panels). Finally, biopsies from human right appendages (RAps) displayed considerably higher crest reliefs with 6–7 SSM/crest (Supplementary material online, Figure S4C).

Overall, these results unveiled the existence of a compartment-dependence of the CM surface crest relief.

3.4 CMs establish lateral communications with neighbour CMs through crest–crest direct physical interactions

Another intriguing question was the organization of the lateral surface crest architecture between neighbour CMs. Unexpectedly, lateral crest interlocking was identified in the mouse (Figure 4A) and cow-LV biopsies (Supplementary material online, Figure S5). When screening numerous TEM micrographs in the LV from mice, cows, and humans and in contrast

Figure 2 Continued

number/crest in mouse LV was assessed using Spearman test. (F) Qualitative comparison of crest subpopulations according to their SSM number content in mouse, rat, cow, and human LV ($n = 7$ mice, 3–7 CMs/mouse, $n = 5$ rats, 3–10 CMs/rat, $n = 2$ cows, 14–16 CMs/cow, and $n = 1$ human, 16 CMs). (G) Linear correlation between crest height and sarcomere length in mouse or rat LV was assessed using Spearman test. (H) Crest heights measured in (B) were quantified in mouse and rat LV relative to the sarcomere length. The statistical significance between mouse and rat LV was assessed using unpaired Student's *t*-test ($*P < 0.05$).

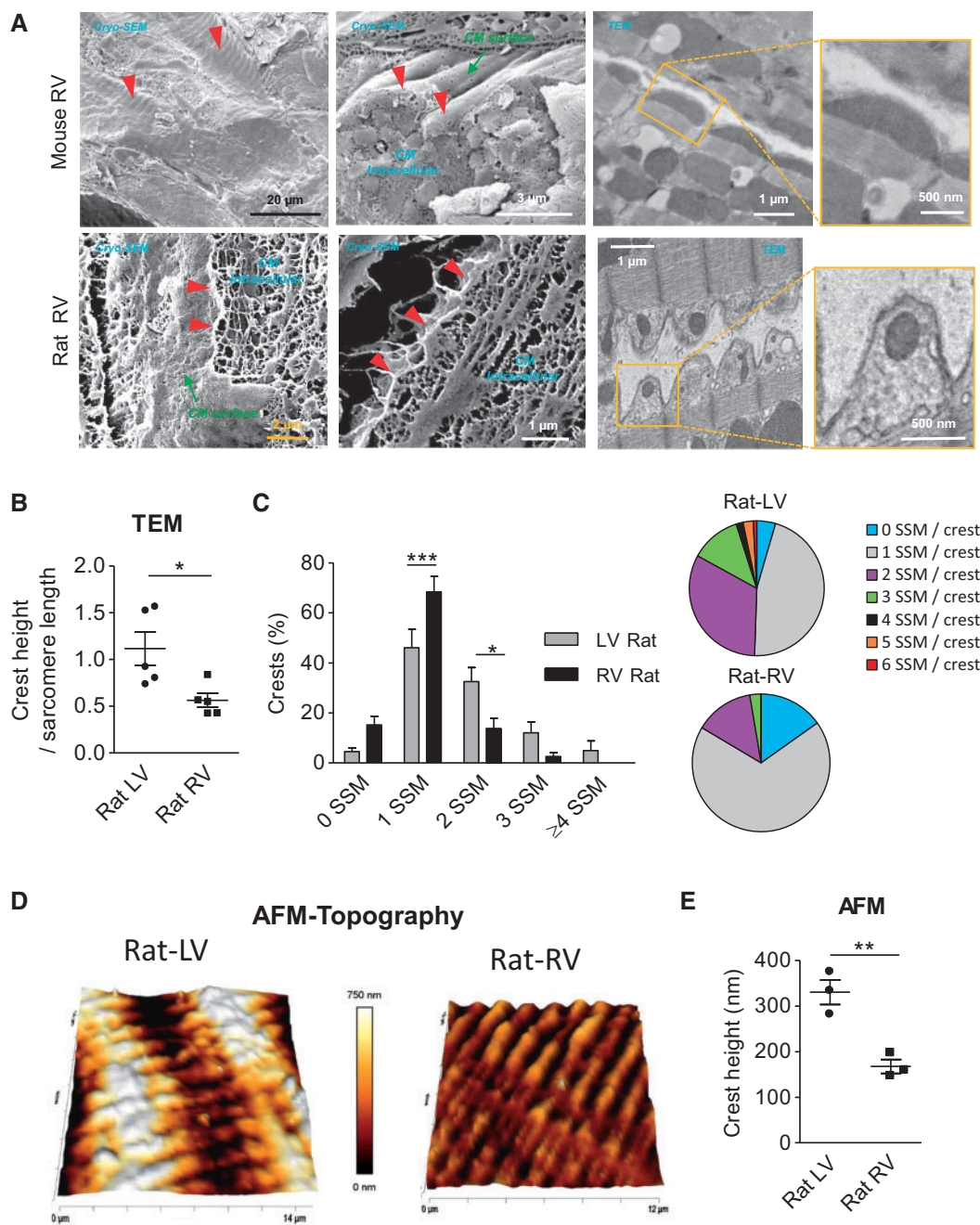


Figure 3 CM lateral surface crest relief differs in heart compartments. (A) Cryo-SEM or TEM micrographs showing CM surface crest relief of mouse (upper panels) or rat RV myocardium (lower panels). Red arrows indicate CM surface crests. (B) Quantification of crest heights on TEM micrographs ($n = 5$ rats, VG/3-10 CMs/rat/237 total crests; VD/5-15 CMs/rat/239 total crests). The statistical significance between rat LV and RV was assessed using unpaired Student's t -test (** $P < 0.01$). (C) Quantification of crest subpopulations in rat LV and RV according to their SSM number content ($n = 5$ rats) (left panel). The statistical significance between rat LV and RV was assessed using two-way ANOVA followed by a Bonferroni post-test (* $P < 0.05$; ** $P < 0.001$). (Right panel) Pie chart representation of CM surface crest subpopulations between rat LV and RV. (D) Representative image of a 3D AFM-based topography height map of CM surface from rat LV or RV. (E) Quantification of crest heights on AFM-height maps ($n = 3$ rats, 2–4 CMs/rat). The statistical significance between rat LV and RV was assessed using unpaired Student's t -test (** $P < 0.01$).

to the assumption, we identified electron dense structures, typical of tight junction between two adjacent lateral sarcolemma, thus indicating direct physical interactions between lateral nearby CMs (Figure 4B and Supplementary material online, Figure S6). Distinct crest structures could

not be visualized in these pictures due to the general poor quality of the human biopsies due to deterioration (delayed fixation and no ice use). Compared with the ID, the tight junctions at the CM lateral side are scattered and intermittent. Indeed, when first depicted on a 70 nm-thick

MET micrograph, the next tight junction could be found only 40 serial micrographs ($\sim 2.8 \mu\text{m}$) further.

Tight junction structures, indicative of a direct physical communication in between cells, are generally only accepted from the ID standpoint in the CM. However, the existence of lateral CM interactions through tight junctions reconciles the presence of specific tight junctional proteins like Claudin-5 or zonula occludens-1 (ZO-1) that we and others have previously described at the CM lateral membrane.^{3,4,10,11} It also corroborates the presence of Ephrin-B1, a cell–cell communication protein from the Eph-Ephrin system, that we previously reported as a direct partner of Claudin-5 at the CM lateral face.³ To ascertain the direct lateral physical interactions between CMs and to get a better overview of these lateral tight junctions on a larger 3D cardiac tissue image, we conducted super-resolution microscopy on mouse heart cryo-sections using SIM (Structured Illumination Microscopy) or STED (Stimulated Emission Depletion Microscopy) microscopy, allowing 100 and 70 nm xy resolution respectively when compared with the classical 250 nm resolution in confocal microscopy. Both Claudin-5 and Laminin-2, a specific basement component of the CM lateral membrane, have been examined in immunofluorescence microscopy. When first visualized through classical confocal microscopy (Supplementary material online, Figure S7A), some wavy lateral structures (yellow arrows) could be observed at the surface of CMs in the mouse myocardium, in agreement with the presence of the crests. Compared with Laminin-2, the Claudin-5 staining was punctuated, with some Claudin-5–Claudin-5 interactions in *trans* that could be perceived in tissue zones with interlateral space enlargement (Claudin-5 zoom).

When considering higher resolution using SIM microscopy (Figure 4C), the CM surface crests could be better appreciated and Claudin-5–Claudin-5 interactions could be clearly depicted in between two adjacent CMs. These interactions were irregular along the CM surface in a 2D image, thus reminiscing a zip. We also confirmed the presence of a continuous basement membrane layer as reflected by the Laminin-2 staining at the CM surface by opposition to the intermittent Claudin-5 expression. STED imaging further confirmed these 2D observations (Figure 4D) but allowed us to go deeper in the z resolution imaging of the 3D lateral space between two CMs. The reconstituted 3D images of a 2 μm thick tissue (Supplementary material online, Video and Figure 4E) highlighted direct interactions between two Claudin-5 in *trans* via their extracellular part in the inter-lateral membrane space between two adjacent CMs. The bottom view of the CM surfaces also indicated the interruption of the Laminin-2 staining at Claudin-5 contacts throughout the surface (Supplementary material online, Figure S7B). These intermittent Claudin–Claudin interactions thus create an intricate lateral meshwork at the sarcolemmal surface of the CMs.

3.5 CMs exhibit loss of surface crest architecture and lateral crest–crest interactions in cardiac diseases

We next questioned the organization of lateral crests at the CM surface in the cardiac pathophysiology.

Using TEM, we examined the CM surface crests in Ap collected from patients (Methods). As shown in Figure 5A (upper panels), the RAp from Patient 3, which demonstrated a dilated atrium but a preserved ejection fraction, partially preserved the CM surface crest relief with the presence of SSM (left panel), although some of the crests were SSM-free (presence of autophagosome) (right panel). In contrast, Patient 5 with both left atrium (LA) and left ventricular dilation (Figure 5A, left lower

panels) or Patient 4 with LA dilatation and heart failure (Figure 5A, lower panels) mostly lost their CM surface crests (flat surface) with only residual atrophic (SSM shrinking) or giant SSM (SSM fusion). Thus, the loss of CM surface crests could be a general feature in cardiac pathophysiology which could entail a subsequent loss of the lateral CM contacts and a lateral space enlargement. However, given the poor biopsy sampling, the advanced disease state but also the associated medication of these patients, it was impossible to conclude on the impact of a particular parameter on the crest disruption in such multifactorial context.

To better evaluate a potential link between the pathological cardiac state and its impact on crest contacts, we conducted an experimental model of pressure overload-induced hypertrophy in mice (Transverse Aortic Constriction, TAC-model) (Figure 5B). Fifteen days after TAC, the mice developed a significant hypertrophy as shown by echocardiography (Figure 5C) and CM area quantification (Figure 5D) with no major contractile dysfunction (Figure 5C). The SIM microscopy of heart biopsies revealed some interstitial fibrosis as indicated by collagen III immunostaining in between adjacent CMs in the left ventricular myocardium (Supplementary material online, Figure S8). Correlatively, we found that in TAC mice, all the CMs partially or totally lose their surface crests compared with sham mice as indicated by the MET quantifications (Figure 5E). It is thus tempting to conclude on a role of hypertrophy on the disruption of lateral crest–crest contacts. However, it is difficult to ascertain this conclusion since TAC generally leads to concomitant hypertrophy and fibrosis development. Given that the surface crests anchored to Z-lines and that the crest–crest contacts ensure tight lateral CM–CM connections, the loss of the CM surface crests could affect the overall cardiac tissue cohesion but also the myofibril and myofiber lateral alignment (Supplementary material online, Figure S9). Consistent with this hypothesis, the cardiac tissue from TAC mice demonstrated a substantial Z-lines misalignment as indicated by the α -actinin staining as well as a myofibril and myofiber disorganization reflected by the Troponin-T imaging (Supplementary material online, Figure S10).

4. Discussion

We have characterized, at a high resolution, the 3D-CM surface organization within cardiac tissue. The salient findings are: (i) the compartment- and species-dependent coverage of the CM lateral surface by periodic bulged rows filled with SSM, (ii) the physical interaction of the bulged rows with those of adjacent CMs through Claudin-5-dependent tight junction strands. These results reconcile the identification of atypical proteins from cell–cell communication at the CM lateral membrane, that we and others previously reported.^{3,4,10,11}

4.1 Lateral crest structure-function: cardiac tissue cohesion hypothesis

The existence of spatially distinct subpopulations of mitochondria in the CM is accepted.¹² Despite several attempts to determine the specific role of SSM,¹² given their extreme sensitivity to cardiac tissue handling procedures as reported here or the CM isolation previously described⁵ and the lack of a stringent marker to distinguish SSM from IFM, the question remains open. The existence of SSM beneath the CM lateral plasma membrane is established but was never quantified, and the incidence of such peculiar cell surface architecture at the cellular and tissue 3D-scale has not been previously explored. In contrast to the initial assumption of spherical mitochondria,¹² 3D-reconstitution beam images indicated that SSM exhibit a similar elongated morphology to IFM. However, they are

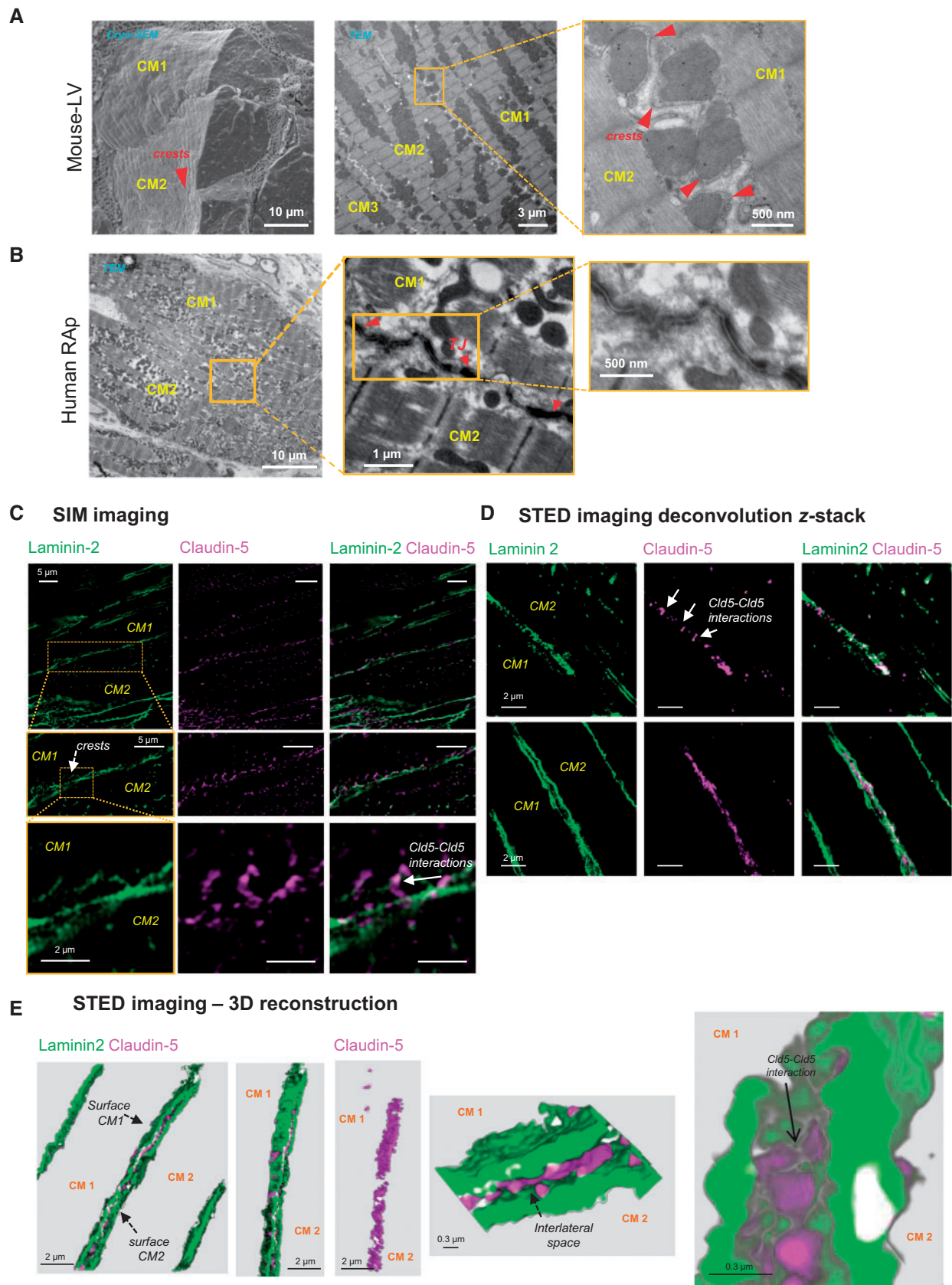


Figure 4 Neighbour CMs establish lateral physical contacts through tight junction-dependent crest-crest interactions. (A) Cryo-SEM or TEM micrographs of mouse left ventricular myocardium showing close interactions between lateral surface crests of two adjacent CMs. (B) TEM micrographs of human RAP (Patient 1) showing longitudinal electron-dense tight junctions between lateral membranes of two adjacent CMs (red arrows). (C and D) High-resolution SIM

orientated perpendicularly to the IFM rows and lie on the outer myofibril layer. The SSM end-to-end arrangement shapes the overall lateral surface of the CM into periodic bulged rows. This particular 3D-organization of the CM surface has not been depicted in living CMs in AFM.⁵ In contrast, periodic crest/hollow structures were observed rather than rows. This most likely arises from a technical issue because SSM are highly prone to shrinking once the CM separated from the cardiac tissue. Thus, in isolated CMs, elongated SSM tend to shrink and adopt a more round morphology, thus leading to periodic ball structures at the CM surface as previously indicated by AFM.⁵

More strikingly, the discovery of lateral physical connections between adjacent CMs through surface crest–crest interaction changes our view on the spatial architecture of the cardiac tissue because to date, CM–CM direct interactions have been restricted to the ID. Thus, while the ID most likely supports the longitudinal stretch of intracellular myofibrils, the lateral stretch provided by crest–crest interactions could ensure their stacking during contraction. Indeed, the CM surface crests are directly anchored to the Z-lines of the outer myofibril layer and the lateral crest–crest contacts could thus stretch and allow the alignment of the Z-lines from the overall myofibrils (Supplementary material online, Figure S9A). From a tissue standpoint, lateral CM interactions could ensure the alignment between myofibers (Supplementary material online, Figure S9B), thus providing and strengthening the overall tissue cohesion which is necessary to adapt to the physical constraints during cyclic heart beats. In agreement with this hypothesis, the loss of CM surface crests was observed in the barometric stress-mouse model. Interestingly, this could influence the compliance of the cardiac compartments during the cardiac cycle by generating a 3D meshing more or less closely dependent on the crest height. It could thus underlie the well-known higher compliance of the RV with lower crest relief than the LV with higher crests.¹³

4.2 Lateral crest structure-function: sarcomere relaxation control hypothesis

An intriguing finding is the dependence of the relief of CM surface crest on the cardiac compartment among the different mammalian species and on the species for a compartment. CM crest relief could correlate with the compartment pressure with, for example, higher crest relief in the LV than in the RV. However, the observation of crests in compartments with almost no pressure, such as cow atria and human appendage, does not fit with this hypothesis. From the species perspective, higher crest reliefs were identified in higher mammals (mouse < rat < cow < human) and were inversely correlated with the heart rate. In agreement, the decrease in the heart rate during postnatal cardiac maturation¹⁴ tightly correlates with SSM and cell surface crest maturation.⁵

At the sarcomere level, the longitudinal movements of myofibrils control both heart contraction (systole) and relaxation (diastole). In this study, we found a significant correlation between the crest height and the sarcomere length, consistent with the crest anchorage to the Z-lines and most likely arguing for a role of the crests in the control of the contractile state of the sarcomere. To date, the lateral function of the sarcomere was only attributed to the cell surface costamere connecting the extracellular barometric stress to the intracellular and compensatory myofibril contraction.²

Intuitively, when considering the crest–crest lateral interactions and mechanical forces involved, they should not interfere with sarcomere contraction (Figure 6). In contrast, lateral forces generated by the crest–crest interface may restrain the sarcomere relaxation length during diastole to preserve crest–crest interactions. A mechanosensing mechanism could control this phenomenon because the CM is highly recognized as a mechanosensor machinery.¹⁵ Thus, the crest height could dictate the sarcomere relaxation state with higher crests enabling a maximal relaxation length and time (Figure 6). In such hypothetical model, crests could thus impact the isovolumic relaxation time (IVRT), the dynamic phase of the diastole. In agreement, the LV-IVRT is longer in higher mammalian species (horse: 90 ± 17 ¹⁶ ms, human: $\sim 74 \pm 7$ ms,¹⁷ pig: 80 ± 15 ms¹⁸) than in smaller animals (cat: 48.0 ± 6.8 ms,¹⁹ rat: 25.5 ± 6.26 ms²⁰; mouse: 14 ± 0.6 ms²⁰) and we showed that CMs from human-Ap or cow-LV myocardium harbour higher surface crest relief than those of rats or mice. The IVRT theory is also consistent with the compartment-dependence of the crest relief. Indeed, even if the existence of a dynamic phase of atrial diastole, despite recent suggestions,²¹ is not clearly established, we found that the mouse crests in atrium < RV < LV. This also suggests that the human atrial IVRT should be substantially lower or nonexistent than the RV (53.7 ± 9.16 ms²²) or LV (IVRT $\sim 74 \pm 7$ ms¹⁷). Finally, the IVRT and thus the active diastolic control of the sarcomere could coordinate all CMs from a compartment in a similar relaxation length to synchronize the subsequent passive diastolic phase. Noticeably, the diastolic sarcomere length–crest height relationship is further reinforced by the indirect correlation between the CM surface crest height⁵ and diastolic function,²³ which both concomitantly mature within the first three weeks postnatal in rodents. In the future, animal models that specifically lack SSM and CM surface crests should help validate this hypothesis. The CM surface crest structure in animal models of diastolic dysfunction with a preserved ejection fraction and specific IVRT lengthening would also be interesting to investigate.

4.3 Disruption of the lateral crest architecture in cardiac pathologies

From a pathological standpoint, human data clearly highlight CM surface crest defects in patients with dilated cardiomyopathies in the absence of systolic dysfunction and their worsening with an altered ejection fraction. Moreover, in an experimental mouse model of hypertrophy with no major contractile function defects, we also identified a major loss of CM surface crests.

Specifically, we noted here and previously in hearts from mice with post-ischaemic myocardial dysfunction,⁵ considerable SSM shrinking, SSM fusion and mitophagy events, which are all indicative of mitochondria dysfunctions.²⁴ Interestingly, mitochondria shrinking has long been described as a metabolic adaptation of the mitochondria to its environment.²⁵ Given the dramatic changes in cardiac metabolism that occur in most cardiac diseases, SSM localized in the frontline at the CM surface could thus be affected first. Consequently, SSM shrinking could be indicative of pathological metabolic changes. Similarly, specific changes of cardiac metabolism have been described in mice depending on the anaesthesia–euthanasia procedure²⁶ which could support the substantial euthanasia-SSM sensitivity reported in this study.

Figure 4 Continued

(C) and STED (D) immunofluorescence imaging of Laminin-2 and Claudin-5 at the lateral surface of CMs in the cardiac tissue from mouse myocardium and highlighting cell surface crests (wavy surface) and Claudin-5/Claudin-5 interactions *in trans*. (E) 3D-reconstitution of STED imaging showing Claudin-5 interactions in the CM–CM lateral space and connecting the two lateral faces of neighbour CMs reflected by the Laminin-2 staining (See also Supplementary material online, movie).

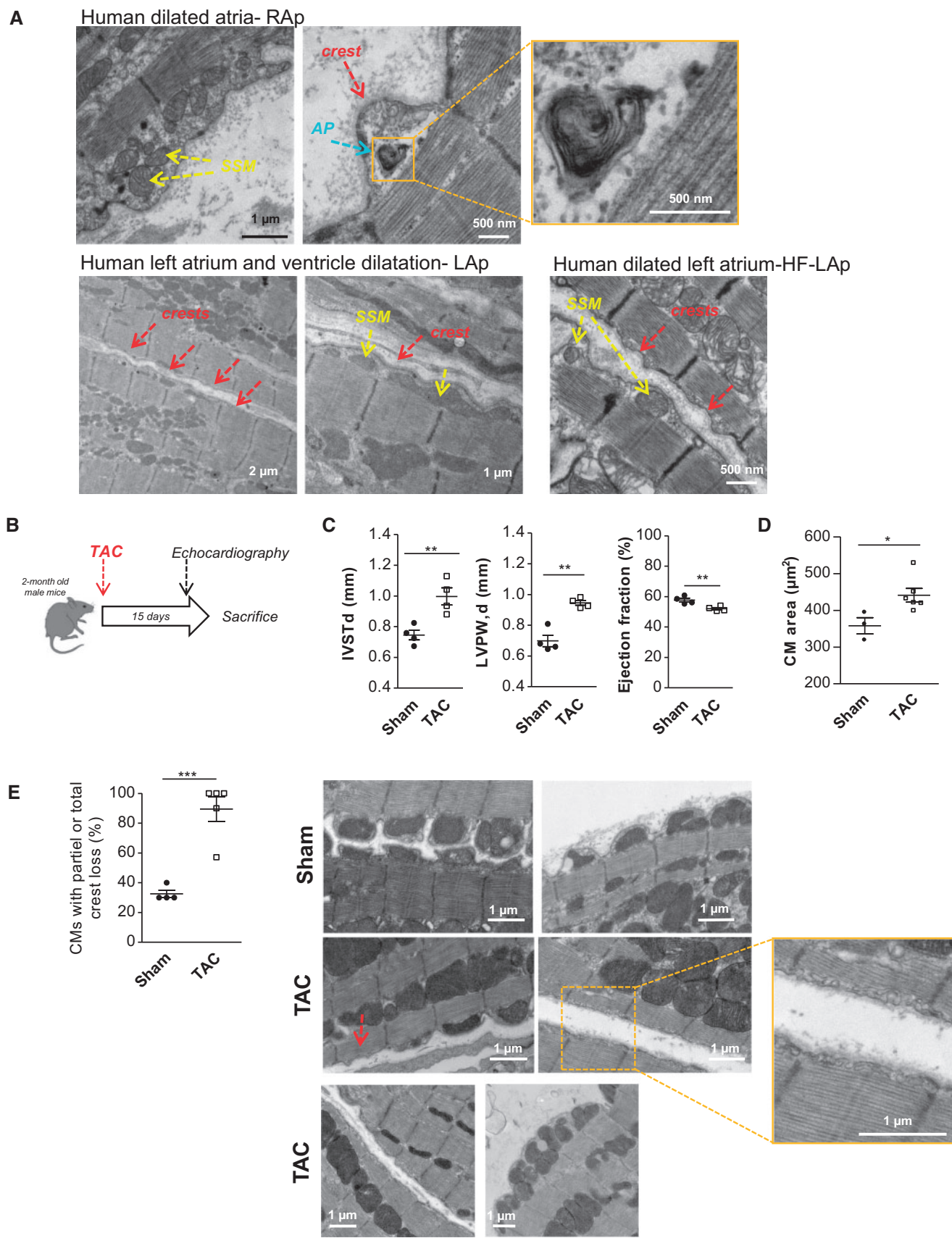


Figure 5 CM surface crest defects in cardiac diseases. (A) TEM micrographs of human Ap from hearts with various cardiac defects. (Upper panels) Dilated RAP with preserved ejection fraction (EF) (Patient 3) showing small surface crests with small SSM (yellow arrows) and autophagosomes (AP-blue arrows) in the smallest SSM-free crests. (Left lower panels) Dilated left appendage (Lap) with left ventricular dilatation with normal EF (Patient 5) showing total loss of

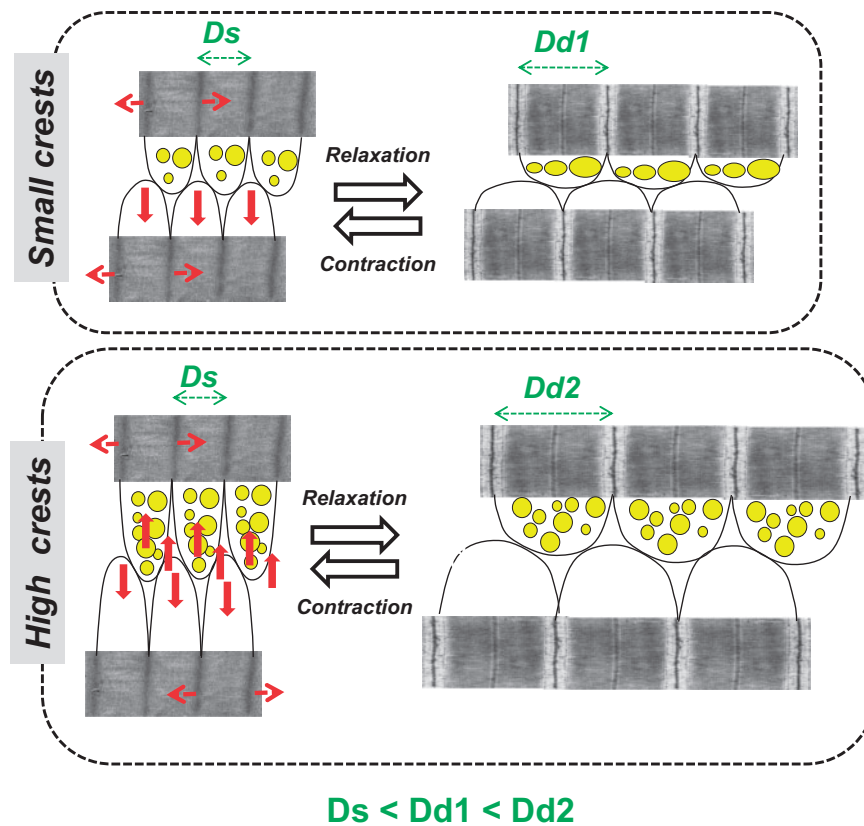


Figure 6 Hypothetic model for a role of the CM surface crests in the control of the cardiac relaxation. From a physical standpoint, the CM surface crest heights and their physical interaction with crests from neighbour CMs should dictate the control of the sarcomere relaxation length during diastole. Indeed, small crest heights (low SSM number) (*upper panels*) at the CM surface should restrict sarcomere lengthening (Dd1-distance in diastole) to preserve crest–crest interactions, whereas in contrast, higher crest heights (*lower panels*) should ensure longer sarcomere stretching (Dd2 > Dd1 > Ds-distance in systole).

These results also confirm that the CM surface crest defects could be a more general event that occurs in heart failure as previously reported.^{5,7} It also suggests that the crest loss at the CM surface could be an initial event participating to the later development of heart failure. In line with this hypothesis, we previously demonstrated in isolated CMs from failing mouse hearts (ischaemic hearts) that the early loss of surface crests evolves over time to a substantial CM plasma membrane fragility that could lead to its ultimate disruption.⁵ The loss of CM crests could thus participate to the CM death through necrosis, a specific process

relying on the CM plasma membrane fragility but also a specific hallmark of patients with end-stage heart-failure.²⁷ Moreover, we also previously showed that such crest loss precedes T-Tubule disorganization in an ischaemic heart model, which is considered as a general hallmark of end-stage heart failure from different origins.²⁸ Thus, given that T-Tubule network reflects intracellular invaginations of the CM lateral membrane, the initial crest–crest contact disruption and crest loss could constitute an initial common hallmark that evolves over time to the setting of heart failure. Finally, whether crest loss could specifically underlie the initial

Figure 5 Continued

surface crests (red arrows) and absence of SSM or, in some cases, very small but giant elongated SSM (yellow arrows) and the loss of Z-line crest anchorage. (*Right lower panel*) Dilated LAp with heart failure (*Patient 4*) showing flat CM lateral surface (red arrows) and absence or very small SSM (yellow arrows). In all cases, the loss of lateral physical contacts between CMs is observed. (B) Experimental mouse model of barometric stress-induced cardiac hypertrophy through transaortic constriction (TAC). (C) Echocardiography-based analysis of diastolic interventricular septal thickness (IVST, d), diastolic left ventricular posterior wall thickness (LVPW, d), and EF measured 15 days after TAC. (D) (*left panel*) *In situ* quantification of CM area (Sham $n = 3$ mice, TAC $n = 6$ mice; 100–150 CMs/group). (E) The partial or total crest loss were quantified in TEM micrographs and data are expressed as percentage of the total CMs observed (Sham $n = 4$ mice; TAC $n = 5$ mice; 10 CMs/group). Statistical analysis was performed using Fisher's exact test, *** $P < 0.001$. (*Right panels*) Illustrative TEM micrographs of LV showing the partial or total loss of surface crests in the TAC model compared with sham mice. Some CM surface heaps related to the loss of the periodic lateral membrane anchorage to the Z-line and thus to the assembly of SSM from different neighbour crests were also noted.

ventricular diastolic dysfunction based on our molecular hypothesis (Figure 6) and precede the systolic dysfunction will need future investigations.

Supplementary material

Supplementary material is available at *Cardiovascular Research* online.

Acknowledgements

The authors thank E. Blasco and K. Ramondou for technical assistance and the ANEXPLO platform for help with echocardiography. We are also grateful to TRI Genotoul network facilities, specifically to Elodie Véga for technical assistance for SIM imaging (*Cellular Imaging Facility-I2MC/TRI platform*), the *Cellular Imaging Facility-CPTP/TRI platform* for STED imaging, and the 'Centre de Microscopie Electronique Appliquée à la Biologie-Faculté de Médecine Rangueil/TRI platform'.

Conflict of interest: none declared.

Funding

This work was supported by the 'Fondation Bettencourt Schueller', the 'Fondation pour la Recherche Médicale' (FRM DEQ20170336733 to C.G.) and the «Fondation de France».

References

- Yang X, Pabon L, Murry CE. Engineering adolescence: maturation of human pluripotent stem cell-derived cardiomyocytes. *Circ Res* 2014;**114**:511–523.
- Samarel AM. Costameres, focal adhesions, and cardiomyocyte mechanotransduction. *Am J Physiol Heart Circ Physiol* 2005;**289**:H2291–H2301.
- Genet G, Guilbeau-Frugier C, Honton B, Dague E, Schneider MD, Coatrieux C, Calise D, Cardin C, Nieto C, Payré B, Dubroca C, Marck P, Heymes C, Dubrac A, Arvanitis D, Despas F, Altié MF, Seguelas MH, Delisle MB, Davy A, Sénard JM, Pathak A, Galés C. Ephrin-B1 is a novel specific component of the lateral membrane of the cardiomyocyte and is essential for the stability of cardiac tissue architecture cohesion. *Circ Res* 2012;**110**:688–700.
- Sanford JL, Edwards JD, Mays TA, Gong B, Merriam AP, Rafael-Fortney JA. Claudin-5 localizes to the lateral membranes of cardiomyocytes and is altered in utrophin/dystrophin-deficient cardiomyopathic mice. *J Mol Cell Cardiol* 2005;**38**:323–332.
- Dague E, Genet G, Lachaize V, Guilbeau-Frugier C, Fauconnier J, Mias C, Payré B, Chopinet L, Alsteens D, Kasas S, Severac C, Thireau J, Heymes C, Honton B, Lacampagne A, Pathak A, Sénard JM, Galés C. Atomic force and electron microscopic-based study of sarcolemmal surface of living cardiomyocytes unveils unexpected mitochondrial shift in heart failure. *J Mol Cell Cardiol* 2014;**74**:162–172.
- Nikolaev VO, Moshkov A, Lyon AR, Miragoli M, Novak P, Paur H, Lohse MJ, Korchev YE, Harding SE, Gorelik J. Beta2-adrenergic receptor redistribution in heart failure changes cAMP compartmentation. *Science* 2010;**327**:1653–1657.
- Lyon AR, MacLeod KT, Zhang Y, Garcia E, Kanda GK, Lab MJ, Korchev YE, Harding SE, Gorelik J. Loss of T-tubules and other changes to surface topography in ventricular myocytes from failing human and rat heart. *Proc Natl Acad Sci USA* 2009;**106**:6854–6859.
- Chopinnet L, Formosa C, Rols MP, Duval RE, Dague E. Imaging living cells surface and quantifying its properties at high resolution using AFM in QI mode. *Micron* 2013;**48**:26–33.
- Hendgen-Cotta UB, Esfeld S, Jastrow H, Totzeck M, Altschmied J, Goy C, Haendeler J, Winterhager E, Rassaf T. Mouse cardiac mitochondria do not separate in subsarcolemmal and interfibrillar subpopulations. *Mitochondrion* 2018;**38**:1–5.
- Mays TA, Binkley PF, Lesinski A, Doshi AA, Quaille MP, Margulies KB, Janssen PM, Rafael-Fortney JA. Claudin-5 levels are reduced in human end-stage cardiomyopathy. *J Mol Cell Cardiol* 2008;**45**:81–87.
- Swager SA, Delfin DA, Rastogi N, Wang H, Canan BD, Fedorov VV, Mohler PJ, Kilic A, Higgins RS, Ziolo MT, Janssen PM, Rafael-Fortney JA. Claudin-5 levels are reduced from multiple cell types in human failing hearts and are associated with mislocalization of ephrin-B1. *Cardiovasc Pathol* 2015;**24**:160–167.
- Hollander JM, Thapa D, Shepherd DL. Physiological and structural differences in spatially distinct subpopulations of cardiac mitochondria: influence of cardiac pathologies. *Am J Physiol Heart Circ Physiol* 2014;**307**:H11–14.
- Walker LA, Buttrick PM. The right ventricle: biologic insights and response to disease. *Curr Cardiol Rev* 2009;**5**:22–28.
- Ostchega Y, Porter KS, Hughes J, Dillon CF, Nwankwo T. Resting pulse rate reference data for children, adolescents, and adults: United States, 1999–2008. *Natl Health Stat Report* 2011;1–16.
- Dostal DE, Feng H, Nizamutdinov D, Golden HB, Afrozeh SH, Dostal JD, Jacob JC, Foster DM, Tong C, Glaser S, Gerilechaogetu F. Mechanosensing and regulation of cardiac function. *J Clin Exp Cardiol* 2014;**5**:314.
- Verheyen T, Declodet A, Clercq D, Loon G. Cardiac changes in horses with atypical myopathy. *J Vet Intern Med* 2012;**26**:1019–1026.
- Nagueh SF, Appleton CP, Gillebert TC, Marino PN, Oh JK, Smiseth OA, Waggoner AD, Flachskampf FA, Pellikka PA, Evangelisa A. Recommendations for the evaluation of left ventricular diastolic function by echocardiography. *Eur J Echocardiogr* 2008;**10**:165–193.
- Reiter U, Reiter G, Manninger M, Adelsmayr G, Schipke J, Alogna A, Rajces A, Stalder AF, Greiser A, Muhlfield C, Scherr D, Post H, Pieske B, Fuchsjaeger M. Early-stage heart failure with preserved ejection fraction in the pig: a cardiovascular magnetic resonance study. *J Cardiovasc Magn Reson* 2016;**18**:63.
- Disatian S, Bright JM, Boon J. Association of age and heart rate with pulsed-wave Doppler measurements in healthy, nonsedated cats. *J Vet Intern Med* 2008;**22**:351–356.
- Horgan S, Watson C, Glezeva N, Baugh J. Murine models of diastolic dysfunction and heart failure with preserved ejection fraction. *J Card Fail* 2014;**20**:984–995.
- Rai DB. The dynamic function of the atrial diastole of the heart and motion of venous valves in humans. *Int J Angiol* 2013;**22**:37–44.
- Fahmy Elnoamany M, Abdelraouf Dawood A. Right ventricular myocardial isovolumic relaxation time as novel method for evaluation of pulmonary hypertension: correlation with endothelin-1 levels. *J Am Soc Echocardiogr* 2007;**20**:462–469.
- Zhou YQ, Foster FS, Parkes R, Adamson SL. Developmental changes in left and right ventricular diastolic filling patterns in mice. *Am J Physiol Heart Circ Physiol* 2003;**285**:H1563–H1575.
- Ong SB, Hausenloy DJ. Mitochondrial morphology and cardiovascular disease. *Cardiovasc Res* 2010;**88**:16–29.
- Packer L. Metabolic and structural states of mitochondria. I. Regulation by adenosine diphosphate. *J Biol Chem* 1960;**235**:242–249.
- Overmyer KA, Thonusin C, Qi NR, Burant CF, Evans CR. Impact of anesthesia and euthanasia on metabolomics of mammalian tissues: studies in a C57BL/6j mouse model. *PLoS One* 2015;**10**:e0117232.
- Silver M, Gotlieb AI, Schoen FR. *Cardiovascular Pathology*. Churchill Livingstone, 3rd ed, July 2, 2001.
- Ibrahim M, Gorelik J, Yacoub MH, Terracciano CM. The structure and function of cardiac t-tubules in health and disease. *Proc Biol Sci* 2011;**278**:2714–2723.